On the discrepancy between local and average structure in the fast Na^+ ionic conductor $Na_{2.9}Sb_{0.9}W_{0.1}S_4$

Oliver Maus[a,b], Matthias T. Agne[a], Till Fuchs[c], Paul S. Till[a], Björn Wankmiller[b,d], Josef Maximilian Gerdes[d], Rituraj Sharma[e], Michael Heere[f], Niina Jalarvo[g], Omer Yaffe[e], Michael Ryan Hansen[b,d], Wolfgang G. Zeier*[a,b,h]

[a]*Institute of Inorganic and Analytical Chemistry, University of Münster, D-48149 Münster, Germany*

[b]*International Graduate School for Battery Chemistry, Characterization, Analysis, Recycling and Application (BACCARA), University of Münster, D-48149 Münster, Germany*

[c]*Institute of Physical Chemistry, Justus-Liebig-University Giessen, Heinrich-Buff-Ring 17, D-35392 Giessen, Germany*

[d]*Institute of Physical Chemistry, University of Münster, D-48149 Münster, Germany*

[e]*Department of Chemical and Biological Physics, Weizmann Institute of Science, Rehovot, 76100 Israel*

[f]*Technische Universität Braunschweig, Institute of Internal Combustion Engines, Hermann-Blenk-Straße 42, D-38108 Braunschweig, Germany*

[g]*Neutron Science Division, Oak Ridge National Laboratory, Oak Ridge, TN 37830, USA*

[h]*Institut für Energie- und Klimaforschung (IEK), IEK-12: Helmholtz-Institut Münster, Forschungszentrum Jülich, D-48149 Münster, Germany*

Corresponding author email: wzeier@uni-muenster.de

Abstract

Aliovalent substitution is a common strategy to improve the ionic conductivity of solid electrolytes for solid state batteries. The substitution of SbS_4^{3-} by WS_4^{2-} in $Na_{2.9}Sb_{0.9}W_{0.1}S_4$ leads to a very high ionic conductivity of 41 mS/cm at room temperature. While pristine Na_3SbS_4 crystallizes in a tetragonal structure, the substituted $Na_{2.9}Sb_{0.9}W_{0.1}S_4$ crystallizes in a cubic phase at room temperature based on its X-ray diffractogram. Here, we show by performing pair distribution function analyses and static single-pulse ^{121}Sb NMR experiments that the short-range order of $Na_{2.9}Sb_{0.9}W_{0.1}S_4$ remains tetragonal despite the change in the Bragg diffraction pattern. Temperature-dependent Raman spectroscopy revealed changed lattice dynamics due to the increased disorder in the Na^+ substructure lead to dynamic sampling causing the discrepancy in local and average structure. While showing no differences in the local structure, when compared to pristine Na_3SbS_4, quasi-elastic neutron scattering and solid-state ^{23}Na nuclear magnetic resonance measurements revealed drastically improved Na^+ diffusivity and decreased activation energies for $Na_{2.9}Sb_{0.9}W_{0.1}S_4$. The obtained diffusion coefficients are in very good agreement with theoretical values and long-range transport measured by impedance spectroscopy. This work demonstrates the importance of studying the local structure of ionic conductors in order to fully understand their transport mechanisms, a prerequisite for the development of faster ionic conductors.

Introduction

Rechargeable batteries are nowadays not only relevant for electrical vehicles and electronic devices but are more and more considered as large-capacity storage solutions in power grids. All-solid state batteries are promising candidates to achieve high energy densities[1] and enable the use of high capacity anodes such as lithium metal[2,3] or silicon alloys.[4,5] Growing research over the last years led to the discovery of solid electrolyte materials such as the thiophosphate based $Li_{10}GeP_2S_{12}$[6,7] and Li_6PS_5X (X = Cl, Br, I)[8–10] as well as the chloride based Li_3MCl_6 (M = Y, Er, In),[11–13] which all achieve ionic conductivities in the range of liquid electrolytes.[14] Sodium solid state batteries are gaining increasing interest[15,16] as a more sustainable alternative to lithium ion batteries due to the much higher abundance of sodium, the opportunity to avoid the use of critical elements like nickel and cobalt,[17] as well as higher ionic conductivities of the solid ionic conductors.[1,18] For highly performing solid-state batteries it is crucial to have an electrochemically stable solid electrolyte with high ionic conductivity above 10 mS/cm,[19] which can be achieved in sulfide-based Na^+ solid ionic conductors.[20,21]

Some of the most promising Na^+ ion conductors are based on the sodium thiophosphate Na_3PS_4.[22] The Na_3PnCh_4 (*Pn* = P, Sb; *Ch* = S, Se) material class crystallizes either in a cubic high temperature phase with $I\bar{4}3m$ space group symmetry or in a tetragonal phase with $P\bar{4}2_1c$ space group symmetry (see Figure 1).[23] In the cubic structure, the PnS_4^{3-} tetrahedra form a body-centered structure with Na^+ ions filling the octahedral voids. In the tetragonal polymorph, the tetrahedra are rotated along the [111] axis and the *c* axis is slightly elongated. Additionally, a fraction of Na^+ ions gain a free positional parameter and shift along the *c* axis, resulting in a two Na^+ positions instead of one as found in the cubic polymorph.[24]

Due to the absence of vacant Na^+ sites in the structure and the lack of stable interstitial sites, stoichiometric and defect-free Na_3PS_4 and Na_3SbS_4 are relatively poor ionic conductors, however, reported conductivities indicate that synthesized materials already have a certain vacancy density.[25,26] Aliovalent substitution can improve the ionic transport significantly,[27–29] in particular the substitution of SbS_4^{3-} by WS_4^{2-} increases the ionic conductivity by orders of magnitude.[21,30] In fact, the composition $Na_{2.9}Sb_{0.9}W_{0.1}S_4$ is one of the fastest Na^+ ion conductor discovered so far, achieving a conductivity of 41 mS/cm at room temperature, which allows its use in all-solid state batteries.[20]

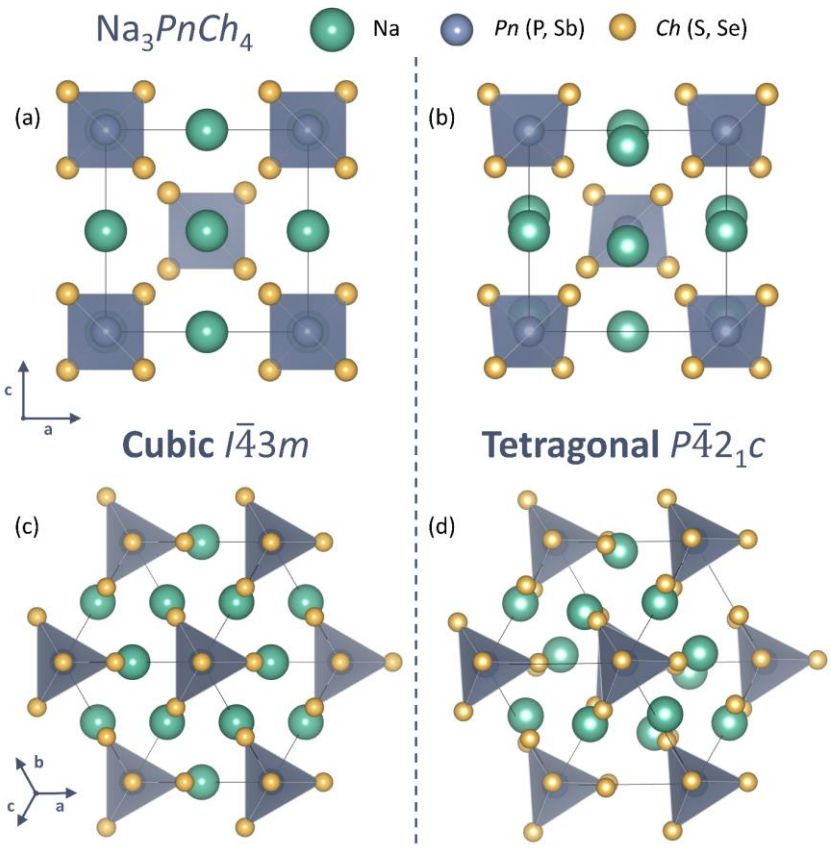

Figure 1: a) *Cubic and* ***b)*** *tetragonal structure of* Na_3PnCh_4 *viewed along the* [*100*] *axis. The projections along the* [*111*] *axis of the* ***c)*** *cubic and* ***d)*** *tetragonal structure show the rotated* $PnCh_4^{3-}$ *polyhedra of the tetragonal polymorph as well as the two crystallographic* Na^+ *positions.*

And yet, despite the importance of vacancies, the exact factors underlying the high conductivity are still not completely understood. A recent theoretical study could not find any evidence for a paddlewheel mechanism of the anionic polyhedral and therefore concluded that the increase in conductivity is solely caused by the introduction of vacancies, as initially proposed.[31,32] It was also suggested that the higher electronegativity of W^{6+} leads to smaller WS_4^{2-} tetrahedra, thereby facilitating better diffusion of Na^+ ions by reducing the structural bottleneck.[32] Experimentally, the introduction of tungsten leads to a reduction of the unit cell volume and induces a structural change along the series.[20]

While the unsubstituted Na_3SbS_4 exists in the tetragonal phase at room temperature, $Na_{2.9}Sb_{0.9}W_{0.1}S_4$ is reported to crystallize in a cubic phase based on X-ray diffraction. Currently, it is assumed that the cubic structure allows for slightly better three-dimensional diffusion pathways in contrast to the tetragonal structure.[21] However, previous investigations in this class of materials have shown discrepancies between the local average and long-range average

crystalline structures.[33,34] For instance, when Na_3PS_4 is prepared via a ball-milling approach it appears to have an average cubic structure, but tetragonal domains are evident at the local scale using pair-distribution function analysis. It seems that by introducing vacancies and disorder due to the highly energetic ball milling process, the tetragonal motif is disrupted and either averaged to a cubic symmetry overall or straining the grains significantly.[33]

Hence, the fast ionic transport in $Na_{2.9}Sb_{0.9}W_{0.1}S_4$ associated with a large vacancy concentration leads to the following question: Could there be a similar influence of the vacancies on the local structure as previously reported for Na_3PS_4? At this stage, little is known about how these differences in local and average structure affect the transport properties on a local and long-range scale. Considering the possibility of discrepancies between the local and average structure in defective crystalline materials is an important and poorly understood topic in ionic conductors. Herein, we systematically study the local structure and ionic transport properties of $Na_{2.9}Sb_{0.9}W_{0.1}S_4$, which has chemically introduced Na^+ vacancies, and compare it to Na_3SbS_4, which nominally does not have any vacancies, as well as $Na_{2.9}Sb_{0.95}W_{0.05}S_4$ to complete the series. By using a combination of X-ray Bragg diffraction and X-ray pair distribution function analyses, solid-state ^{23}Na and ^{121}Sb nuclear magnetic resonance spectroscopy, Raman spectroscopy, impedance spectroscopy and quasi-elastic neutron scattering, we investigate the average global and local structure as well as the long-range and local ionic transport behavior.

Our observations show that vacancy introduction leads to a dynamic sampling over a local scale tetragonal structural motif, that strongly modulates the average long-range structure to appear cubic. The in-depth transport characterization shows that, irrespective of the structural changes, the local and average transport properties show similar trends of increasing ionic transport during substitution. Clearly, local and average structures can deviate slightly, supporting the need to study the local short-range structure of fast ionic conductors as these are more accurate representations of the material compared to their average long-range structures.

Experimental/Methods

Synthesis. $Na_{2.9}Sb_{0.9}W_{0.1}S_4$, $Na_{2.95}Sb_{0.95}W_{0.05}S_4$, and Na_3SbS_4 were synthesized by solid-state synthesis under inert conditions following the synthesis protocol from Fuchs *et al.*[20] According to the degree of W-substitution, stoichiometric amounts of Na_2S (Sigma-Aldrich, 2% excess), Sb_2S_3 (Sigma-Aldrich), elemental sulfur S_8 (Sigma-Aldrich) and WS_2 were scaled, ground in a mortar for 20 minutes, pressed into pellets and filled into dried quartz ampules. The ampules were sealed under vacuum and put into a horizontal tube furnace where the reaction took place at 823 K for 20 hours after heating up at a rate of 30 K per hour.

X-ray diffraction and Rietveld refinement. The X-ray diffraction data were recorded using a Stoe STADI P diffractometer (Mo $K_{\alpha1}$ radiation: λ = 0.70930 Å, Ge 111 monochromator) in Debye-Scherrer geometry with a Dectris MYTHEN2 1K detector. The samples were measured in sealed glass capillaries over a 2θ-range of 4-45° with a scanning rate of 1° per minute.

Phase analyses and Rietveld refinements were carried out using TOPAS academics V7.[35] R_{wp}, R_{exp}, and goodness of fit (*gof*) were used as fit indicators to assess the quality of the refinement. The profile was refined by (1) a scale factor, (2) 6 free background coefficients of a Chebyshev polynomial function, (3) peak shape parameters of a modified Thompson−Cox−Hastings pseudo-Voigt function[36], (4) a full axial model to account for the asymmetry of the peak due to axial divergence as described by Cheary *et al.*[37], (5) a zero point offset, (6) the lattice parameters. With fixed profile, (7) the fractional atomic coordinates and subsequently (8) isotropic atomic displacement parameters were fit.

Pair distribution function analyses. Total scattering data was recorded using a Stoe STADI P diffractometer (Ag $K_{\alpha1}$ radiation: λ = 0.55941 Å, Ge 111 monochromator) in Debye-Scherrer geometry with four Dectris MYTHEN2 1K detectors as described by Thomae *et al.*[38] The samples were measured in sealed glass capillaries over a *Q*-range of 0.8-20.5 $Å^{-1}$ for 24 h.

Data reduction was carried out using PDFgetX3 with a *Q*-range cutoff of Q_{max} = 18 $Å^{-1}$.[39] Small box modeling was performed using PDFgui.[40] The PDF data analysis was adapted from previous work on Na_3PS_4.[33] The data was first fitted in an *r*-range of 4-20 Å where (1) scale factor, (2) correlated motion factor, (3) lattice parameters, (4) atomic positions, and (5) isotropic atomic displacement parameters were subsequently refined. In order to take the correlated motion of the SbS_4^{3-} unit into account, the scale factor, correlated motion factor, and the atomic positions were separately refined for the *r*-range of 2-4 Å as previously shown to be necessary for these materials.[33,41]

Raman spectroscopy. Raman spectra of the samples were acquired using a custom-built Raman system with a Horiba FHR-1000 spectrometer. 785 nm diode laser (TOPTICA Photonics AG) was used for excitation at a power of 1.5 mW, focused on the sample using a 10x objective (Nikon). Two volume holographic notch filters (each having OD>4 rejection with a spectral cut off ±7 cm^{-1} around 785 nm) remove the Rayleigh-scattered light and allow measurements covering both Stokes and anti-Stokes sides of the spectrum. Low-temperature measurements were carried out in an optical cryostat (Janis, USA) evacuated to 10^{-5} Torr. A Linkam TS1000EV optical furnace was used to measure the Raman spectra above room temperature. The sample capillaries were directly loaded on the cryostat/Linkam stage for measurement. The heating rate was kept constant at 5 K/min, with an equilibration time of 10 minutes for each temperature.

A multi-Lorentz line shape convolved with a Bose-Einstein distribution (n_{BE}) factor was used to fit the Raman spectra at each temperature to determine the peak position and broadening using a customized code in Igor Pro 8 as in Ref 41.[42] The experimental Raman spectrum can be expressed as a combination of Debye and a damped Lorentz oscillator term as

$$I_{\mathrm{exp}}(\nu, \nu_i, \Gamma_i) = c_{\mathrm{BE}}(\nu)\left(\frac{c_0|\nu|\Gamma_0}{\nu^2+\Gamma_0^2} + \sum_{i=1}^{n} c_i \frac{|\nu||\nu_i|\Gamma_i^2}{\nu^2\Gamma_i^2 + (\nu^2-\nu_i^2)^2}\right)$$

where ν is the spectral shift, ν_i are the resonance frequencies of the Lorentz oscillators, Γ_0 and Γ_i are the damping coefficients of the Debye relaxation and Lorentz oscillators respectively, c_0 and c_i are unitless fitting parameters for the intensities of the Debye and Lorentz oscillator components respectively. The spectral shift ν, the parameters ν_i and Γ_i are in wavenumber units. $c_{\mathrm{BE}}\ (\nu)$ includes the Bose-Einstein distribution of thermal population including a Bose-Einstein distribution factor. The spectral artifacts due to the notch filter around 0 cm^{-1} were omitted and only the Stokes scattering was fitted to find the positions and widths of the peaks.

Impedance spectroscopy. As recently performed by Fuchs *et al.*,[20] impedance measurements were carried out using an *SP300* potentiostat from Biologic in a frequency range from 100 mHz to 7 MHz within a temperature range from -40 °C to 60 °C. The temperature was controlled by the *WKL 64* climate chamber from Weiss. For the measurements, the samples were isostatically pressed at 380 MPa to obtain dense pellets (> 80% relative density) and a 200 nm thick gold layer was deposited on both sides of each pellet as electrical contacts. Aluminum current collectors were attached to the pellets using Kapton tape. To avoid contact with air, the whole

setup was pouched in argon atmosphere. Measurements were controlled using the software ECLab V 13.0, while the obtained spectra were analyzed with RelaxIS 3.

Quasi-elastic neutron scattering (QENS). QENS data were recorded at the BASIS backscattering spectrometer at the Spallation Neutron Source of the Oak Ridge National Laboratory.[41] Si111 analyzers were used with 6.4 Å wavelength and 60 Hz chopper operation mode. Samples (6-8 g) were filled under inert conditions into aluminum sample holders (1 mm-spaced double wall cylinder) and sealed mechanically with aluminum foil as a gasket. The sample holder was mounted in the spectrometer where a closed-cycle refrigerator with a hot stage was used to measure at 50, 300, 400, 500 and 600 K for 3 h respectively. Data reduction was carried out using the Mantid software package. The data was normalized against a Vanadium standard and grouped in Q bins of width 0.1 $Å^{-1}$ over a range of 0.2 to 2.0 $Å^{-1}$ and energy bins of width 0.8 μeV over a range of −100 to 100 μeV. Using the Dave software package, the reduced data were fitted using the following model[43]:

$$S(Q,E) = \left(A\delta(E) + B\frac{\pi\Gamma(Q)}{\Gamma(Q)^2 + E^2} \right) * \ R(Q,E) + C(Q,E)$$

with $A\delta(E)$ as the elastic contribution, the second term as the Lorentzian corresponding to the quasi-elastic broadening, both of which are convoluted with *R(Q,E)* the resolution function taken to be the nominally diffusion-less signal measured at 50 K, and adding a linear background function *C(Q,E)*. From the Lorentzian function we extracted the half-width half-maximum Γ of the quasi-elastic broadening. The Q dependence of Γ was then fitted by the Chudley-Elliott model to obtain the jump distance, residence time and, thereby, the diffusion coefficient at each temperature.[44]

Nuclear magnetic resonance (NMR) spectroscopy. Static saturation-recovery ^{23}Na NMR experiments were performed on a Bruker Avance III 300 spectrometer equipped with a wide-bore magnet operating at 7.05 T using a VTN broadband NMR probe. The powder samples were transferred into cylindrical zirconia rotors with an outer diameter of 4 mm under argon atmosphere. All ^{23}Na experiments were conducted at a resonance frequency of 79.4 MHz with a radio-frequency pulse length of 2.5 μs for a 90° pulse, corresponding to a nutation frequency of 100 kHz. The length of the recovery delay was incremented with three steps per decade from 10 μs to 21.544 s. The Fourier transformed signals were integrated and the signal intensity curves were fitted using an exponential saturation function with a stretching exponent. The static saturation-recovery ^{23}Na NMR experiments were performed in a temperature range of 220 K to 400 K in 20 K steps. The temperature of the sample was regulated by using a nitrogen

gas flow and electrical heating. In the temperature range between 200 K and 290 K an *Air Jet* XR compressor-based cooling system from SP Scientific (FTS Systems) and in the temperature range of 320 K to 440 K an uncooled nitrogen gas flow was used to stabilize the temperature. ^{1}H NMR spectra of methanol (200 K to 290 K) and ethylene glycol (320 K to 440 K) were recorded to calibrate the temperature with the occurring shifts in signal frequency.

Static single-pulse ^{121}Sb NMR spectra were recorded on a Bruker AVANCE NEO spectrometer equipped with a wide bore magnet operating at 11.76 T using a VTN broadband NMR probe. The ^{121}Sb chemical shift range was referenced to solid K[SbF_6] at 0 ppm. Pulse length and power level were set so that a 0.5 µs pulse corresponded to a flip angle of π/12. Definitions of the tensor parameters are given in the Supporting Information. The ^{121}Sb NMR experiments were conducted at three temperatures of 205 K, 296 K and 423.5 K as well as in 20 K steps around the respective phase transition temperatures observed from XRD (Figure S4), except for Na_3SbS_4 where the phase transition temperature lies above the hardware limit.

Results and discussion

Local tetragonal structure of $Na_{2.9}Sb_{0.9}W_{0.1}S_4$

In order to investigate the effect of aliovalent substitution on the local structure, $Na_{3-x}Sb_{1-x}W_xS_4$ with a substitution degree of x = 0, 0.05 and 0.1 was prepared via solid-state synthesis. The X-ray diffractograms against the scattering vector Q of the obtained compounds are shown in Figure 2a. As expected, the pristine Na_3SbS_4 exhibits a characteristic splitting of the (200), (211) and (220) reflections corresponding to the tetragonal $P\bar{4}2_1c$ structure. The splitting is much less pronounced for 5% of W-substitution, and not observed at all for $Na_{2.9}Sb_{0.9}W_{0.1}S_4$, indicating a transition from the tetragonal to the cubic phase as recently observed.[20,21] In addition, the (212) reflection, characteristic for the tetragonal polymorph, is absent for $Na_{2.9}Sb_{0.9}W_{0.1}S_4$. Figure S1d shows how the lattice parameters a and c approach each other with increasing substitution until they have the same value for the 10% substituted sample. In addition, the dihedral angle that geometrically describes the rotation of the PnS_4^{3-} tetrahedra decreases from 4° for Na_3SbS_4 to 0° for $Na_{2.9}Sb_{0.9}W_{0.1}S_4$ (Figure S2), again showing the transition to a cubic structure in the average structure. The Rietveld refinement (Figure S1c) confirms the cubic structure with $I\bar{4}3m$ space group symmetry for $Na_{2.9}Sb_{0.9}W_{0.1}S_4$. However, as Bragg reflections are the sum of all constructive interferences of X-rays scattered over the whole sample, it can therefore only detect average structural features which are periodic with

enough coherency. As most models of diffusing ions are based on jumps from one lattice site to the next, the local short-range order is significant for ionic transport, but might differ from the average crystal structure.

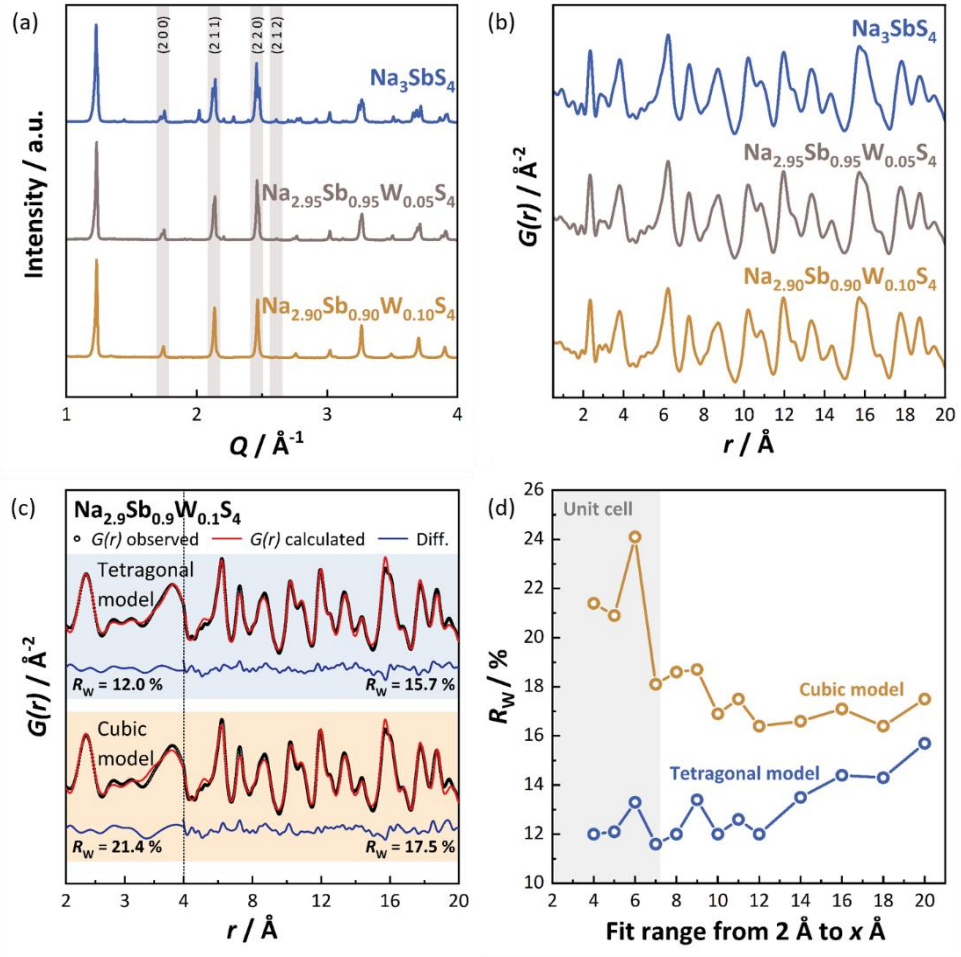

Figure 2: a) *X-ray diffractograms of $Na_{3-x}Sb_{1-x}W_xS_4$ with a substitution degree of x = 0, 0.05 and 0.10. The decreased splitting of the (200), (211), and (220) reflections as well as the absence of the (212) reflection suggests a transition from tetragonal to cubic symmetry.* ***b)*** *Pair distribution functions of $Na_{3-x}Sb_{1-x}W_xS_4$ showing no significant difference in the local structure of all three compositions.* ***c)*** *Comparison of the pair distribution function of $Na_{2.9}Sb_{0.9}W_{0.1}S_4$ analyzed by using a cubic and a tetragonal model, showing better fit residuals for the tetragonal structural model.* ***d)*** *Fit residuals of small box modelling as a function of the fitted r-range show that the tetragonal model results in a better fit for all ranges and in particular within ranges of one unit cell.*

Therefore, pair distribution function (PDF) analyses are used to assess the local structure of the materials. The total scattering of the sample is measured and a histogram of atom-atom

distances is obtained via Fourier transformation, in which the local structure is dominant in the low-*r* region and the average crystal structure is more and more represented as *r* increases. Figure 2b shows the PDF data of the three compositions where, in contrast to their Bragg diffraction patterns, no significant differences can be observed. By performing small box modelling of the data for $Na_{2.9}Sb_{0.9}W_{0.1}S_4$ using a cubic and a tetragonal model (Figure 2c), discrepancies to the average Bragg data can be found. The region between 2-4 Å is much better described by the tetragonal model with a R_w value of 12.0% compared to 21.4% for the cubic model. Fitting the PDF over an increasing *r*-range shows that the tetragonal model results in a much better fit, especially within the ranges of one unit cell (Figure 2d). The difference between the two models decreases for larger *r*-ranges but for all ranges the tetragonal model results in lower fit residuals. This is in line with the work by Krauskopf *et al*.[33] that also showed much better residuals in the low-*r* range for the tetragonal model of milled Na_3PS_4, compared to the cubic phase. Performing the data reduction at different Q_{max} cut-off values (Figure S3) corroborates that the differences in the fitting are not caused by termination ripples but can be assigned to structural features. It can be therefore concluded from the PDF data that the short-range order remains tetragonal in the $Na_{3-x}Sb_{1-x}W_xS_4$ substitution series.

These local structural results appear to be in contrast with the Bragg diffraction data in which the global or average crystal structure of $Na_{3-x}Sb_{1-x}W_xS_4$ seems to change from tetragonal to cubic. The comparison of the dihedral angle of the PnS_4 tetrahedra (Figure S2) using the structure model obtained from XRD and PDF underlines how the average structure becomes cubic with substitution while the tetrahedra rotation remains in the local tetragonal structure with dihedral angles that are non-zero. To further understand this behavior, temperature-dependent X-ray diffraction was performed for the three different compositions in a broad temperature range around their respective phase transitions from tetragonal to cubic. Figure S4 shows the Bragg data as a function of composition and temperature, suggesting that the structural phase transition in Na_3SbS_4 is lowered by the substitution and that by a visual inspection a cubic phase exists in $Na_{2.9}Sb_{0.9}W_{0.1}S_4$ above 280 K. While a refinement of the patterns with a tetragonal space group remains in principle possible (see Figure S5), leading to a merging of the c/a ratio to unity at around 300 K.

As the assignment of the space group remains challenging, namely: does the cubic high-temperature, the tetragonal low-temperature or an intermediate phase[23] exist at room temperature? Clearly, another local probe besides PDF is needed. Static single-pulse ^{121}Sb NMR experiments are hence conducted that allow for the discrimination between tetragonal

and cubic symmetry due to the characteristic quadrupole splitting (see Figure 3a). A quadrupole splitting arises if the electric-field gradient at the nuclear site is non-zero, which here is caused by a reduction in local point symmetry. The quadrupole splitting is expressed as the quadrupolar coupling constant C_Q.[45] In all ^{121}Sb NMR spectra recorded for Na_3SbS_4 (Figure 3b) a typical second-order quadrupolar line shape of an axially symmetric quadrupolar interaction tensor was observed, in line with what is expected from the tetragonal point group of the Sb site in the low-temperature phase. For Na_3SbS_4, a decreasing quadrupolar coupling C_Q for ^{121}Sb (Figure 3b) points towards a decrease in the c/a lattice parameter difference leading up to the phase transition (Figure S4).

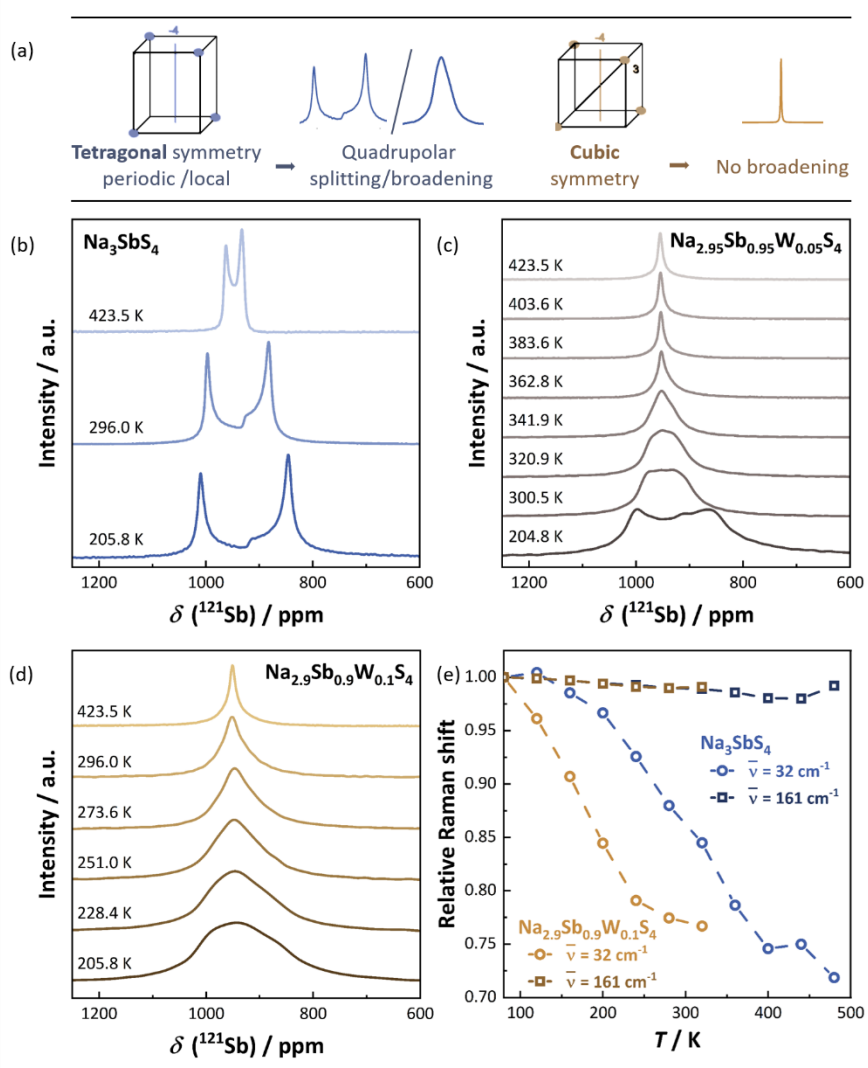

Figure 3: a) *Schematic illustration showing how tetragonal symmetry leads to a quadrupole splitting of the ^{121}Sb NMR signal, which is absent for cubic symmetry.* ***b)*** *Static variable-temperature ^{121}Sb NMR spectra of Na_3SbS_4 showing the characteristic quadrupole splitting for the tetragonal structure. For* ***c)*** *$Na_{2.95}Sb_{0.955}W_{0.05}S_4$ and* ***d)*** *$Na_{2.9}Sb_{0.9}W_{0.1}S_4$, the quadrupole*

splitting is smeared out (broadened) due to increased disorder. With increasing temperature, the quadrupolar splitting decreases but remains visible above the phase transition, indicating local tetragonal symmetry in the cubic average structure. ***e)*** *Fitting the temperature-dependent Raman spectra of* Na_3SbS_4 *and* $Na_{2.9}Sb_{0.9}W_{0.1}S_4$ *shows a shift of the mode at 32* cm^{-1}*. This soft mode is indicative for a diffusion-less transformation that occurs for* $Na_{2.9}Sb_{0.9}W_{0.1}S_4$ *at lower temperatures due to the disorder in the* Na^+ *sublattice.*

A similar trend of decreasing quadrupolar splitting at higher temperatures is observed for $Na_{2.95}Sb_{0.95}W_{0.05}S_4$ and $Na_{2.9}Sb_{0.9}W_{0.1}S_4$ (Figure 3c and 3d), where both phase transition temperatures are within the observable range (see Figure S4). Although the second-order quadrupolar ^{121}Sb NMR line shape is increasingly broadened with higher W-substitution, the reduction of the quadrupolar coupling C_Q is visible by the narrower placement of the signal shoulders (singularities) of the resonance line. Comparing the ^{121}Sb NMR resonances at temperatures equidistant below the respective phase transitions, an average position of the NMR line shape singularities (quadrupolar splitting) can be estimated (Table S8), showing a higher quadrupolar coupling interaction for higher W-substitution. Nevertheless, for both $Na_{2.95}Sb_{0.95}W_{0.05}S_4$ and $Na_{2.9}Sb_{0.9}W_{0.1}S_4$, Figure 3c and 3d, a broadened ^{121}Sb resonance is still observed after the phase transition temperature (Figure S6) to cubic symmetry observed from X-ray diffraction (Figure S4); the broadening of these ^{121}Sb NMR resonances cannot be fit assuming a single Gaussian or Lorentzian line shape, indicating contributions of ^{121}Sb species with stronger than just the average quadrupolar interaction.[46,47] Thus, the occurrence of a non-zero quadrupolar interaction above the phase transition for $Na_{2.95}Sb_{0.95}W_{0.05}S_4$ and $Na_{2.9}Sb_{0.9}W_{0.1}S_4$ shows that local distortions lead to a local tetragonal structure, in line with the observation of local tetragonal structure elements from the PDF analysis.

Explaining the differences in the local and average structure

How can the discrepancy between the cubic average structure and tetragonal local structure be explained? There are three potential reasons for this behavior. (1) The substitution of SbS_4^{3-} by WS_4^{2-} leads to a disorder in the polyanionic framework which may disrupt the tetragonal motif. (2) The higher vacancy density in the Na^+ sublattice increases the mobility of Na^+ ions. The high diffusivity of ions corresponds to large atomic displacement factors that can average out the tetragonal structure motif. (3) Increased disorder leads to changed lattice dynamics, which can entropically stabilize higher-symmetry phases via dynamic sampling.

While the effect of disorder in the polyanion framework (1) cannot be completely ruled out, it is unlikely to be the main driving force for the cubic average structure. Till *et al.* investigated the isoelectronic substitution series of $Na_3P_xSb_{1-x}S_4$ and obtained tetragonal structures for all compositions.[25] Thus, mere polyanion disorder is unlikely to lead to a cubic average structure. In contrast to isoelectronic substitution, the aliovalent substitution of SbS_4^{3-} by WS_4^{2-} leads to an increase in the Na^+ vacancy density (2), and with it much faster ionic transport (see below). In order to explore option (3), here we investigate the lattice dynamics of Na_3SbS_4 and $Na_{2.9}Sb_{0.9}W_{0.1}S_4$ by temperature-dependent Raman spectroscopy. The data can be found in Figure S7. While the overall position and shape of the peaks are similar for the pristine and W-substituted samples, the low-frequency range (< 200 cm^{-1}) of the Raman spectra, which is very susceptible to change in temperature, include two noticeable observations. The first is that the Raman spectra of $Na_{2.9}Sb_{0.9}W_{0.1}S_4$ differs from the spectra of the pristine material as it exhibits a much broader spectral feature centered at around 32 cm^{-1}. This broad spectral feature likely results from second-order Raman scattering of the acoustic phonons that are enhanced by disorder caused by the diffusion of ions in the material.[48–51]

The second observation is that the lowest frequency peak in both materials strongly 'softens' with increasing temperature. To illustrate this, Figure 3e compares the temperature evolution of the lowest-frequency peak position (see the fitting process in the experimental section) to that of another peak in the spectra that is centered around 161 cm^{-1}. These results indicate that the low-frequency peak is likely a soft mode leading to a diffusion-less transformation. Soft modes are common in perovskites crystals,[52–54] $BiVO_4$,[55] and other sodium ion conductors.[43,48] This behavior, where a mode softens but does not reach 0 cm^{-1} before the phase transition occurs, indicates a crossover between displacive and order-disorder phase transitions.[56] Therefore, these results indicate that the cubic phase is only dynamically disordered.[57–59] Figure 3e also shows that the diffusion-less transformation occurs for $Na_{2.9}Sb_{0.9}W_{0.1}S_4$ at lower temperatures than for Na_3SbS_4, corroborating the shift in phase transition temperature found in X-ray diffraction and NMR.

Figure 4 schematically illustrates the potential reasons that may cause the cubic average ordering of the tetragonal structure. Irrespective of the composition, the materials crystallize in the tetragonal polymorph at low temperatures, which will become cubic on average at a certain temperature. At room temperature, $Na_{2.9}Sb_{0.9}W_{0.1}S_4$ is cubic on average while the local probes of PDF and NMR show significant tetragonal distortion. As the soft mode of the tetragonal phase is still visible in the Raman spectra, this indicates dynamic sampling of tetragonal

configurations that on average, appear cubic. The differences in finding the temperatures of this transformation in X-ray diffraction, NMR, and Raman spectroscopy show how complicated the local dynamics are (see Figure S8).

Krauskopf *et al.* reported a similar result in which an increased disorder and vacancies due to ball-milling led to a cubic average structure of Na_3PS_4 while its local structure remained tetragonal.[33] Nevertheless, if the structure is truly cubic or if the high energy ball-milling approach leads to straining of grains and with it an apparent transition to cubic is still up for debate in Na_3PS_4.[41] Here, we can show that chemically induced vacancies strongly affect the average long-range structure in $Na_{2.9}Sb_{0.9}W_{0.1}S_4$ whereas the short-range order is only modulated. The main question that now arises is what the effect of this structural discrepancy on the ionic transport in the material is.

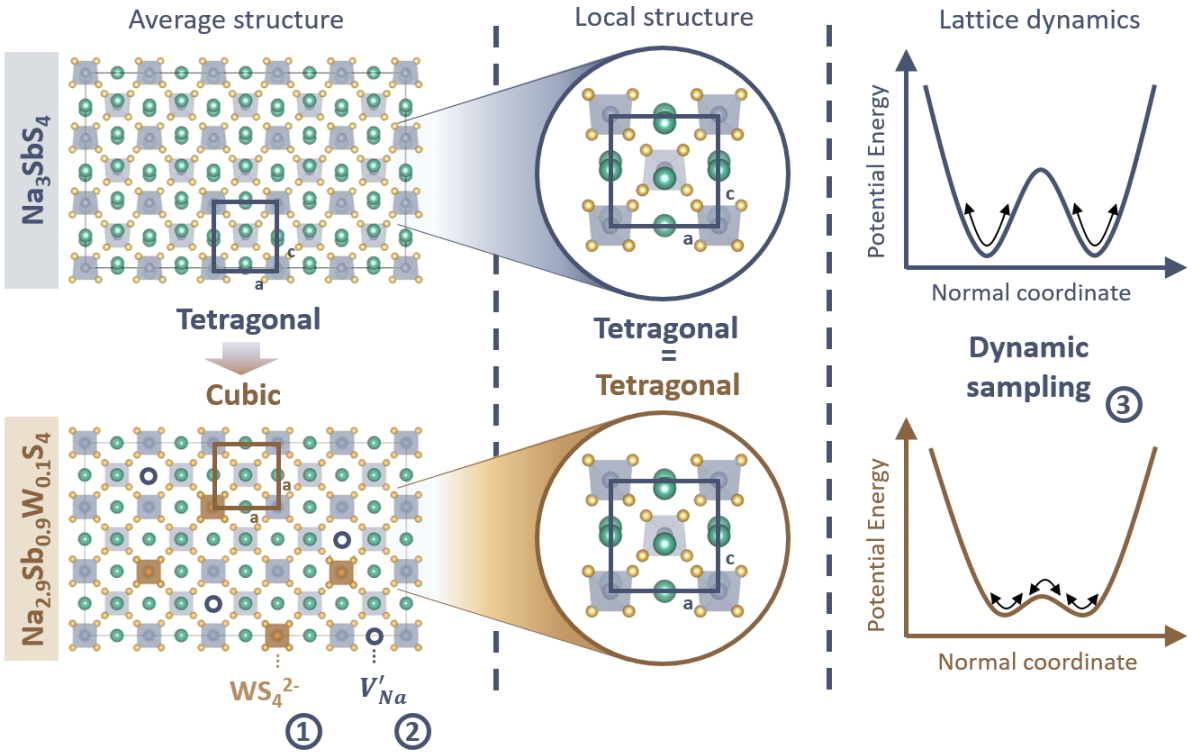

Figure 4: *Schematic illustration how the introduction of WS_4^{2-} polyanions (1), the increase in vacancy density (2) and dynamic sampling (3) lead to a long-range average cubic order in $Na_{2.9}Sb_{0.9}W_{0.1}S_4$ at room temperature while the local short-range order remains tetragonal.*

Local ionic transport

Although long-range ion transport is most important for batteries, ion transport is inherently a local phenomenon at first. Depending on how ion transport is measured, the effective ion mobility across different length-scales can be assessed. Given the similarities in the local structure, we were curious to identify if there were any differences in the behavior of local and long-range ionic transport in $Na_{3-x}Sb_{1-x}W_xS_4$. Electrochemical impedance spectroscopy (EIS) is a powerful and commonly used method to measure ionic conductivity. The representative Nyquist plots of the three compounds are shown in Figure S9a as previously reported by Fuchs *et al*.[20] For Na_3SbS_4, two processes are observed distinguishing the bulk from grain boundary contributions, while for the tungsten-substituted compounds only one process in addition to the blocking electrode is visible. The obtained capacitances for the high-frequency process in a range of 20-34 pF correspond to ionic transport in the bulk material.[20,60] The impedance data show that grain boundaries have negligible contributions, nevertheless, as a global parameter, the obtained ionic conductivities are considered as total conductivities. While the pristine Na_3SbS_4 exhibits a low conductivity of 0.013 ± 0.002 mS/cm, substitution by WS_4^{2-} increases the conductivity multiple orders of magnitude to 34 ± 7 mS/cm for $Na_{2.95}Sb_{0.95}W_{0.05}S_4$ and 41 ± 8 mS/cm for $Na_{2.9}Sb_{0.9}W_{0.1}S_4$. The associated activation energy, obtained from Arrhenius plots in Figure S3b, decreases from 0.25 ± 0.02 eV to 0.21 ± 0.02 eV and 0.19 ± 0.02 eV, respectively. These values obtained by impedance spectroscopy represent the averaged long-range transport over the bulk solid electrolyte. Since the structural investigation shows the discrepancy between the average cubic and the local tetragonal structure, the question arises how aliovalent substitution influences the transport properties on a local scale compared to the long-range average transport data. We therefore performed quasi-elastic neutron scattering and nuclear magnetic resonance spectroscopy to probe the local diffusivity of the materials.

Neutrons can exchange energy with diffusing ions leading to a broadening of the elastic scattering signal, known as quasi-elastic neutron scattering (QENS). Analyzing the spatial distribution of the quasi-elastic broadening allows the determination of diffusion coefficients and by studying the temperature dependence of the observed motion the corresponding activation energies can be extracted.[43,61] Figure 5a and 5b show the QENS spectra at different temperatures of Na_3SbS_4 and $Na_{2.9}Sb_{0.9}W_{0.1}S_4$, respectively. Due to limited measurement time at large-scale facilities, the measurement of the $Na_{2.95}Sb_{0.95}W_{0.05}S_4$ composition was not possible. The non-substituted Na_3SbS_4 shows no discernable quasi-elastic broadening (within the energy resolution of the instrument) and it is not possible to apply the Chudley-Elliott model

that is usually used to quantify local transport properties. The Na^+ diffusivity in this Na_3SbS_4 sample cannot be determined via QENS in contrast to previously reported literature.[62] A likely reason is the different synthesis route which leaded to a very low vacancy density as the small side phase of Na_3SbS_3 indicates.[63] In contrast to pristine Na_3SbS_4, the W-substitution has a dramatic effect on the Na^+ diffusivity. The clearly visible quasi-elastic broadening with increasing temperature shows a remarkably high diffusivity of the W-substituted compound. By fitting the quasi-elastic broadening of $Na_{2.9}Sb_{0.9}W_{0.1}S_4$ by a Lorentzian function (see Figure S10) and extracting the half-width half-maximum Γ of the quasi-elastic broadening, we could apply the Chudley-Elliott model.[44] It is based on the random-walk diffusion model (jump-diffusion on a crystal lattice, from one available site to another) and connects Γ as a function of the scattering vector Q to the jump distance d and residence time τ:

$$\Gamma = \frac{\hbar}{\tau}\left(1 - \frac{\sin(Qd)}{Qd}\right)$$

The Γ-Q plots of $Na_{2.9}Sb_{0.9}W_{0.1}S_4$ in Figure 5c are in good agreement with the Chudley-Elliott model. The obtained residence times and jump distances for each temperature are displayed in Table S8. The jump distances are in the range of the nearest crystallographic Na^+-Na^+ distance of d = 3.62 Å (at 300 K), corresponding to the expected vacancy diffusion mechanism.

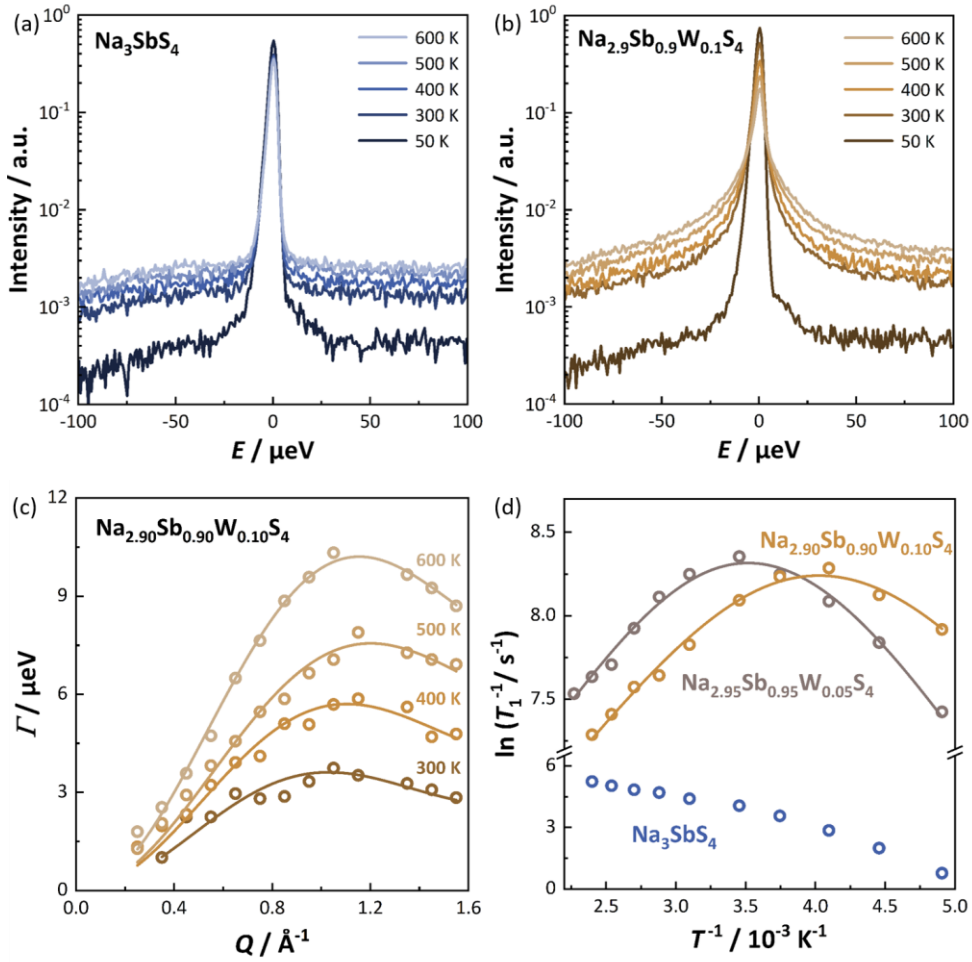

Figure 5: *Temperature-dependent QENS spectra at Q = 0.9 Å^{-1} of* ***a)*** *Na_3SbS_4 and* ***b)*** *$Na_{2.9}Sb_{0.9}W_{0.1}S_4$. While the pristine compound shows no significant change, a clear quasi-elastic broadening can be observed for the substituted sample.* ***c)*** *Chudley-Elliott model of $Na_{2.9}Sb_{0.9}W_{0.1}S_4$ to obtain jump time and distances.* ***d)*** *Saturation-recovery ^{23}Na NMR results of $Na_{3-x}Sb_{1-x}W_xS_4$. The modified BPP model was used to extract the activation energies E_A of Na^+ jumps in $Na_{2.9}Sb_{0.9}W_{0.1}S_4$ and $Na_{2.95}Sb_{0.95}W_{0.05}S_4$ but could not be applied to Na_3SbS_4.*

To further probe the local ionic transport as a function of substitution degree, solid-state ^{23}Na nuclear magnetic resonance (NMR) spectroscopy is used to complement the QENS data. In the investigated Na^+-ion conductors, spin-lattice relaxation of the ^{23}Na nuclei is mainly driven by direct dipole couplings as described by the modified theory of Bloembergen, Purcell, and Pound (BPP).[64,65] The relaxation rate reaches its maximum at the temperature where the frequency of ionic jumps approximately equals the Larmor frequency of the nuclear spins. Thus, by performing saturation-recovery ^{23}Na NMR experiments to determine the spin-lattice relaxation (T_1) times, the BPP model allows the determination of the activation energy E_A and the

preexponential time constant τ_0. From these values the correlation time τ, corresponding to the average time between two jump processes at a given temperature T, can be calculated via:

$$\tau = \tau_0 \cdot \exp\left(\frac{E_A}{k_B T}\right)$$

The Arrhenius plot of the relaxation rate curves of the three $Na_{3-x}Sb_{1-x}W_xS_4$ compositions are displayed in Figure 5d. The maximum of the relaxation rate curve for the non-substituted Na_3SbS_4 lies outside of the measured temperature range and only the low-temperature flank of the relaxation rate curve is observed. This makes it challenging to reliably extract activation barriers of the non-substituted material. However, the long T_1 times indicate the very low diffusivity of Na^+ in pristine Na_3SbS_4, in line with the QENS results. As a result of the W-substitution, T_1 decreases significantly, corresponding to a dramatic increase in ionic diffusivity, see Figure 5d. The relaxation rate curve of the 5% substituted sample reaches its maximum at approximately 284 K and the relaxation rate curve of the 10% substituted sample is shifted to approximately 248 K. The measurable maxima indicate the increasing diffusivity with higher W substitution degree and are rarely observed in Na^+ conductors. Fitting with the BPP model results in activation energies of E_A = 0.10 eV and τ_0 = 17 ps for $Na_{2.95}Sb_{0.95}W_{0.05}S_4$ and E_A = 0.09 eV and τ_0 = 18 ps for $Na_{2.9}Sb_{0.9}W_{0.1}S_4$.

Comparison of local and average transport properties

Both QENS and NMR data already reveal a dramatic increase in local diffusivity due to the aliovalent substitution. The calculation of diffusion coefficients for $Na_{2.9}Sb_{0.9}W_{0.1}S_4$ from the obtained jump times further allows a quantitative assessment of the microscopic diffusivity. The self-diffusion coefficient D can be calculated based on the random walk model from the jump distance d and jump time τ:

$$D = \frac{d^2}{6\tau}$$

Since the random walk model is based on atom-to-atom jumps, we used the nearest crystallographic Na^+ - Na^+ distance (d = 3.62 Å) obtained from the tetragonal local structure model. Figure 6a shows how the obtained diffusion coefficients increase as a function of temperature. The data sets obtained by the two different methods, QENS and NMR, are in remarkably good agreement. We also compared this experimental data with published diffusion coefficients from *ab initio* molecular dynamics (AIMD) calculations for $Na_{2.875}Sb_{0.875}W_{0.125}S_4$.[32] Considering the slightly different stoichiometries that were used for the

theoretical assessment, the theoretical values agree well with the experimental ones. The temperature-dependent diffusion coefficients were used to determine activation barriers for the ionic jumps via an Arrhenius analysis (Figure 6b). The values obtained by NMR measurements and AIMD calculations are very similar with $E_{A,NMR}$ = 0.09 meV and $E_{A,AIMD}$ = 0.10 meV, while QENS obtains a slightly lower activation energy of $E_{A,QENS}$ = 0.05 meV. In summary, the three methods reliably show the high diffusivity of Na^+ in $Na_{2.9}Sb_{0.9}W_{0.1}S_4$ in the order of 10^{-10} m^2/s at 300 K together with a very low activation barrier.

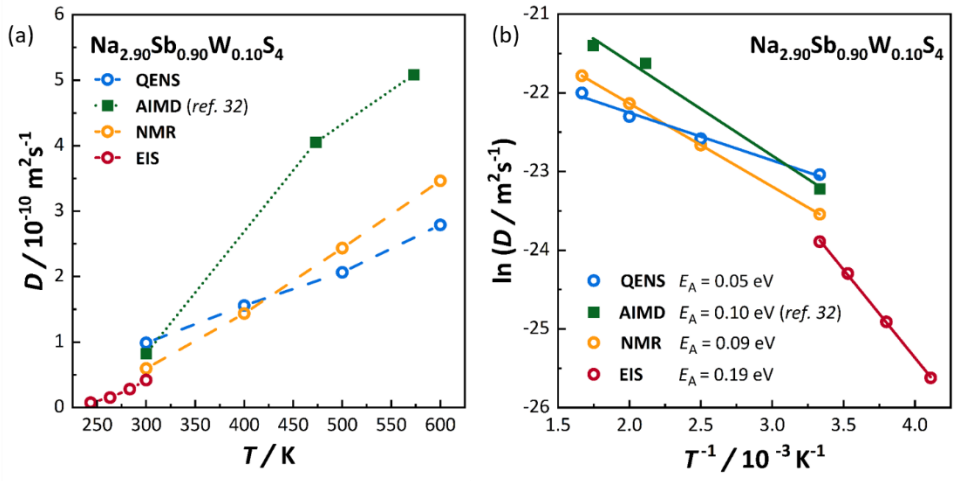

Figure 6: a) *Diffusion coefficients of $Na_{2.9}Sb_{0.9}W_{0.1}S_4$ determined by QENS, NMR, AIMD and EIS are all in the same order of magnitude. The AIMD data were digitized from reference 32.* ***b)*** *Arrhenius plots of diffusion coefficients to determine the associated activation energy of $Na_{2.9}Sb_{0.9}W_{0.1}S_4$.*

Since QENS and NMR measurements, as well as the AIMD calculations, are all considering local ionic jumps without an applied electric field, it is now highly interesting to compare the microscopic diffusivity with the long-range transport data from the impedance spectroscopy. We therefore calculated a diffusion coefficient from the ionic conductivity using the Nernst-Einstein relation with ionic conductivity σ, charge carrier concentration C and charge q assuming a Haven ratio of 1:[66]

$$D = \frac{kT\sigma}{Cq^2}$$

A diffusion coefficient of $4 \cdot 10^{-11}$ m^2/s is obtained at 300 K for $Na_{2.9}Sb_{0.9}W_{0.1}S_4$, which is in the range of the measured value for the local diffusivity. While there is some uncertainty of the calculation due to the necessary assumption of a Haven ratio, even highly correlated motion would only exhibit Haven ratios of 0.2 and with it values still within the same order of

magnitude.[67] Considering the close value of the conductivity based diffusion coefficient to the ones obtained from NMR, QENS and AIMD, it can be concluded that the long-range transport does not differ significantly from its underlying short-range diffusivity. While the substitution only affected the average structure and not the local structure, the local transport properties clearly change in the same manner as the average bulk conductivity.

Comparing the diffusion coefficients of the three different compositions (Figure S11a) shows the dramatic effect that the W-substitution has on the magnitude of ionic diffusivity. Figure S11b shows that also the activation energy decreases with higher substitution degree. While all methods show the same relative trend for the activation energies, the absolute values obtained by EIS are higher than those obtained by QENS and NMR. The reason is that while NMR and QENS are only measuring local ionic jumps, EIS is affected by the microstructure and contacting of the particles. To reduce these effects the pellets were sintered before the measurement, nevertheless, grain boundary contributions must clearly still exist.

The decrease in activation energy suggests that substitution of SbS_4^{3-} by WS_4^{2-} does not only increase the concentration of vacancies as charge carriers but also seems to facilitate local individual ion jumps. In addition to the introduction of vacancies, one may speculate that the more electronegative WS_4^{2-} polyanions might have a potential role in reducing the activation barrier for ionic jumps.[68] Overall, these data confirm that vacancy introduction leads to a dramatic increase in the diffusion coefficient.[31,32]

Conclusions

Aliovalent substitution, and its corresponding vacancy-injection, is a very common strategy to improve the conductivity of solid electrolytes. Here, we showed that the systematic chemical introduction of vacancies by aliovalent substitution of SbS_4^{3-} by WS_4^{2-} in $Na_{3-x}Sb_{1-x}W_xS_4$ leads to a discrepancy between local and average structure. While the short-range order remains tetragonal, the introduction of WS_4^{2-} and vacancies results in an apparent cubic average ordering based on dynamic sampling over tetragonal configurations. Despite the apparent discrepancy of local and global structure, both the microscopic diffusivity and long-range transport are similar as the differently obtained diffusion coefficients are within the same order of magnitude. Compared to pristine Na_3SbS_4, aliovalent substitution dramatically increases the diffusivity for $Na_{2.9}Sb_{0.9}W_{0.1}S_4$ and $Na_{2.95}Sb_{0.95}W_{0.05}S_4$.

Clearly, as chemical changes of the vacancy density, and replacements the polyanionic groups, can lead to large discrepancies in the local structure, other material classes need to be investigated, especially since the modulation of the charge carrier density is the typical approach for improving transport in solid electrolytes. Furthermore, these results may also be relevant for theoretical studies since those focusing on diffusion behavior, as well as interfacial phenomena, are typically based on the average global structures of the materials. Therefore, computational studies might consider basing their models on local structures obtained by pair-distribution function analyses and comparing diffusion coefficients with those obtained via local probes. These implications underline the importance of investigating the local structure to fully understand structure-transport relations in solid ionic conductors.

Supporting Information

Rietveld refinements of the compositions as well as the structural data extracted. Temperature-dependent X-ray diffractograms, fitting results of single-pulse ^{121}Sb NMR spectra as well as Raman spectra are shown. Fitting results of the QENS data, impedance spectra and extracted diffusion coefficients are reported.

Acknowledgments

The research is supported by the International Graduate School for Battery Chemistry, Characterization, Analysis, Recycling and Application (BACCARA), which is funded by the Ministry for Culture and Science of North Rhine Westphalia, Germany. M.T.A acknowledges the Alexander von Humboldt Foundation for financial support through a Postdoctoral Fellowship.

References

(1) Janek, J.; Zeier, W. G. A Solid Future for Battery Development. *Nature Energy* **2016**, *1* (9), 16141.

(2) Krauskopf, T.; Richter, F. H.; Zeier, W. G.; Janek, J. Physicochemical Concepts of the Lithium Metal Anode in Solid-State Batteries. *Chem. Rev.* **2020**, *120* (15), 7745–7794.

(3) Hatzell, K. B.; Chen, X. C.; Cobb, C. L.; Dasgupta, N. P.; Dixit, M. B.; Marbella, L. E.; McDowell, M. T.; Mukherjee, P. P.; Verma, A.; Viswanathan, V.; Westover, A. S.;

Zeier, W. G. Challenges in Lithium Metal Anodes for Solid-State Batteries. *ACS Energy Lett.* **2020**, *5* (3), 922–934.

(4) Tan, D. H. S.; Chen, Y.-T.; Yang, H.; Bao, W.; Sreenarayanan, B.; Doux, J.-M.; Li, W.; Lu, B.; Ham, S.-Y.; Sayahpour, B.; Scharf, J.; Wu, E. A.; Deysher, G.; Han, H. E.; Hah, H. J.; Jeong, H.; Lee, J. B.; Chen, Z.; Meng, Y. S. Carbon-Free High-Loading Silicon Anodes Enabled by Sulfide Solid Electrolytes. *Science* **2021**, *373* (6562), 1494–1499.

(5) Lewis, J. A.; Cavallaro, K. A.; Liu, Y.; McDowell, M. T. The Promise of Alloy Anodes for Solid-State Batteries. *Joule* **2022**, *6* (7), 1418-1430.

(6) Kamaya, N.; Homma, K.; Yamakawa, Y.; Hirayama, M.; Kanno, R.; Yonemura, M.; Kamiyama, T.; Kato, Y.; Hama, S.; Kawamoto, K.; Mitsui, A. A Lithium Superionic Conductor. *Nature Mater* **2011**, *10* (9), 682–686.

(7) Bron, P.; Johansson, S.; Zick, K.; Schmedt auf der Günne, J.; Dehnen, S.; Roling, B. $Li_{10}SnP_2S_{12}$: An Affordable Lithium Superionic Conductor. *J. Am. Chem. Soc.* **2013**, *135* (42), 15694–15697.

(8) Kraft, M. A.; Culver, S. P.; Calderon, M.; Böcher, F.; Krauskopf, T.; Senyshyn, A.; Dietrich, C.; Zevalkink, A.; Janek, J.; Zeier, W. G. Influence of Lattice Polarizability on the Ionic Conductivity in the Lithium Superionic Argyrodites Li_6PS_5X (X = Cl, Br, I). *J. Am. Chem. Soc.* **2017**, *139* (31), 10909–10918.

(9) Zhou, L.; Assoud, A.; Zhang, Q.; Wu, X.; Nazar, L. F. New Family of Argyrodite Thioantimonate Lithium Superionic Conductors. *J. Am. Chem. Soc.* **2019**, *141* (48), 19002–19013.

(10) Deiseroth, H.-J.; Kong, S.-T.; Eckert, H.; Vannahme, J.; Reiner, C.; Zaiß, T.; Schlosser, M. Li6PS5X: A Class of Crystalline Li-rich Solids with an Unusually High Li+ Mobility. *Angewandte Chemie International Edition* **2008**, *47* (4), 755–758.

(11) Schlem, R.; Bernges, T.; Li, C.; Kraft, M. A.; Minafra, N.; Zeier, W. G. Lattice Dynamical Approach for Finding the Lithium Superionic Conductor Li_3ErI_6. *ACS Appl. Energy Mater.* **2020**, *3* (4), 3684–3691.

(12) Liang, J.; Li, X.; Wang, S.; Adair, K. R.; Li, W.; Zhao, Y.; Wang, C.; Hu, Y.; Zhang, L.; Zhao, S.; Lu, S.; Huang, H.; Li, R.; Mo, Y.; Sun, X. Site-Occupation-Tuned Superionic Li_xScCl_{3+x} Halide Solid Electrolytes for All-Solid-State Batteries. *J. Am. Chem. Soc.* **2020**, *142* (15), 7012–7022.

(13) Li, X.; Liang, J.; Luo, J.; Norouzi Banis, M.; Wang, C.; Li, W.; Deng, S.; Yu, C.; Zhao, F.; Hu, Y.; Sham, T.-K.; Zhang, L.; Zhao, S.; Lu, S.; Huang, H.; Li, R.; Adair, K. R.; Sun, X. Air-Stable Li $_3$ InCl $_6$ Electrolyte with High Voltage Compatibility for All-Solid-State Batteries. *Energy Environ. Sci.* **2019**, *12* (9), 2665–2671.

(14) Ohno, S.; Banik, A.; Dewald, G. F.; Kraft, M. A.; Krauskopf, T.; Minafra, N.; Till, P.; Weiss, M.; Zeier, W. G. Materials Design of Ionic Conductors for Solid State Batteries. *Prog. Energy* **2020**, *2* (2), 022001.

(15) Zhou, W.; Li, Y.; Xin, S.; Goodenough, J. B. Rechargeable Sodium All-Solid-State Battery. *ACS Cent. Sci.* **2017**, *3* (1), 52–57.

(16) Zhao, C.; Liu, L.; Qi, X.; Lu, Y.; Wu, F.; Zhao, J.; Yu, Y.; Hu, Y.-S.; Chen, L. Solid-state Sodium Batteries. *Advanced Energy Materials* **2018**, *8* (17), 1703012.

(17) Chu, S.; Guo, S.; Zhou, H. Advanced Cobalt-Free Cathode Materials for Sodium-Ion Batteries. *Chem. Soc. Rev.* **2021**, *50* (23), 13189–13235.

(18) Wang, Y.; Song, S.; Xu, C.; Hu, N.; Molenda, J.; Lu, L. Development of Solid-State Electrolytes for Sodium-Ion Battery–A Short Review. *Nano Materials Science* **2019**, *1* (2), 91–100.

(19) Bielefeld, A.; Weber, D. A.; Janek, J. Modeling Effective Ionic Conductivity and Binder Influence in Composite Cathodes for All-Solid-State Batteries. *ACS Appl. Mater. Interfaces* **2020**, *12* (11), 12821–12833.

(20) Fuchs, T.; Culver, S. P.; Till, P.; Zeier, W. G. Defect-Mediated Conductivity Enhancements in $Na_{3-x}Pn_{1-x}W_xS_4$ (Pn = P, Sb) Using Aliovalent Substitutions. *ACS Energy Lett.* **2020**, *5* (1), 146–151.

(21) Hayashi, A.; Masuzawa, N.; Yubuchi, S.; Tsuji, F.; Hotehama, C.; Sakuda, A.; Tatsumisago, M. A Sodium-Ion Sulfide Solid Electrolyte with Unprecedented Conductivity at Room Temperature. *Nat Commun* **2019**, *10* (1), 5266.

(22) Jia, H.; Peng, L.; Yu, C.; Dong, L.; Cheng, S.; Xie, J. Chalcogenide-Based Inorganic Sodium Solid Electrolytes. *J. Mater. Chem. A* **2021**, *9* (9), 5134–5148.

(23) Seidel, S.; Zeier, W. G.; Pöttgen, R. The Polymorphs of the Na^+ Ion Conductor Na_3PS_4 Viewed from the Perspective of a Group-Subgroup Scheme. *Zeitschrift für Kristallographie - Crystalline Materials* **2020**, *235* (1–2), 1–6.

(24) Krauskopf, T.; Pompe, C.; Kraft, M. A.; Zeier, W. G. Influence of Lattice Dynamics on Na^+ Transport in the Solid Electrolyte $Na_3PS_{4-x}Se_x$. *Chem. Mater.* **2017**, *29* (20), 8859–8869.

(25) Till, P.; Agne, M. T.; Kraft, M. A.; Courty, M.; Famprikis, T.; Ghidiu, M.; Krauskopf, T.; Masquelier, C.; Zeier, W. G. Two-Dimensional Substitution Series $Na_3P_{1-x}Sb_xS_{4-}Se_y$: Beyond Static Description of Structural Bottlenecks for Na^+ Transport. *Chem. Mater.* **2022**, *34* (5), 2410–2421.

(26) Wang, H.; Chen, Y.; Hood, Z. D.; Sahu, G.; Pandian, A. S.; Keum, J. K.; An, K.; Liang, C. An Air-stable Na3SbS4 Superionic Conductor Prepared by a Rapid and Economic Synthetic Procedure. *Angewandte Chemie* **2016**, *128* (30), 8693–8697.

(27) Wang, N.; Yang, K.; Zhang, L.; Yan, X.; Wang, L.; Xu, B. Improvement in Ion Transport in Na3PSe4–Na3SbSe4 by Sb Substitution. *J Mater Sci* **2018**, *53* (3), 1987–1994.

(28) Xiong, S.; Liu, Z.; Rong, H.; Wang, H.; McDaniel, M.; Chen, H. Na3SbSe4−xS x as Sodium Superionic Conductors. *Sci Rep* **2018**, *8* (1), 9146.

(29) Chu, I.-H.; Kompella, C. S.; Nguyen, H.; Zhu, Z.; Hy, S.; Deng, Z.; Meng, Y. S.; Ong, S. P. Room-Temperature All-Solid-State Rechargeable Sodium-Ion Batteries with a Cl-Doped Na_3PS_4 Superionic Conductor. *Sci Rep* **2016**, *6* (1), 33733.

(30) Takayanagi, T.; Nasu, A.; Tsuji, F.; Sakuda, A.; Tatsumisago, M.; Hayashi, A. Mechanochemically Prepared Highly Conductive $Na_{2.88}Sb_{0.88}W_{0.12}S_4$-NaI Composite Electrolytes for All-Solid-State Sodium Battery. *Electrochemistry* **2022**, *90* (4), 047005–047005.

(31) Smith, J. G.; Siegel, D. J. Ion Migration Mechanisms in the Sodium Sulfide Solid Electrolyte $Na_{3-x}Sb_{1-x}W_xS_4$. *Chem. Mater.* **2022**, *34* (9), 4166–4171.

(32) Jalem, R.; Hayashi, A.; Tsuji, F.; Sakuda, A.; Tateyama, Y. First-Principles Calculation Study of Na^+ Superionic Conduction Mechanism in W- and Mo-Doped Na_3SbS_4 Solid Electrolytes. *Chem. Mater.* **2020**, *32* (19), 8373–8381.

(33) Krauskopf, T.; Culver, S. P.; Zeier, W. G. Local Tetragonal Structure of the Cubic Superionic Conductor Na_3PS_4. *Inorg. Chem.* **2018**, *57* (8), 4739–4744.

(34) Patel, S. V.; Banerjee, S.; Liu, H.; Wang, P.; Chien, P.-H.; Feng, X.; Liu, J.; Ong, S. P.; Hu, Y.-Y. Tunable Lithium-Ion Transport in Mixed-Halide Argyrodites $Li_{6-X}PS_{5-}$

$_{x}ClBr_{x}$: An Unusual Compositional Space. *Chemistry of Materials* **2021**, *33* (4), 1435–1443.

(35) Coelho, A. A. TOPAS and TOPAS-Academic: An Optimization Program Integrating Computer Algebra and Crystallographic Objects Written in C++. *Journal of Applied Crystallography* **2018**, *51* (1), 210–218.

(36) Thompson, P.; Cox, D. E.; Hastings, J. B. Rietveld Refinement of Debye–Scherrer Synchrotron X-Ray Data from Al_2O_3. *Journal of Applied Crystallography* **1987**, *20* (2), 79–83.

(37) Cheary, R. W.; Coelho, A. A. An Experimental Investigation of the Effects of Axial Divergence on Diffraction Line Profiles. *Powder Diffraction* **1998**, *13* (2), 100–106.

(38) Thomae, S. L. J.; Prinz, N.; Hartmann, T.; Teck, M.; Correll, S.; Zobel, M. Pushing Data Quality for Laboratory Pair Distribution Function Experiments. *Review of Scientific Instruments* **2019**, *90* (4), 043905.

(39) PDFgetX3: A Rapid and Highly Automatable Program for Processing Powder Diffraction Data into Total Scattering Pair Distribution Functions. **2013**, *46*(2), 560-566.

(40) Farrow, C. L.; Juhas, P.; Liu, J. W.; Bryndin, D.; Božin, E. S.; Bloch, J.; Proffen, T.; Billinge, S. J. L. PDFfit2 and PDFgui: Computer Programs for Studying Nanostructure in Crystals. *Journal of Physics: Condensed Matter* **2007**, *19* (33), 335219.

(41) Famprikis, T.; Kudu, Ö. U.; Dawson, J. A.; Canepa, P.; Fauth, F.; Suard, E.; Zbiri, M.; Dambournet, D.; Borkiewicz, O. J.; Bouyanfif, H.; Emge, S. P.; Cretu, S.; Chotard, J.-N.; Grey, C. P.; Zeier, W. G.; Islam, M. S.; Masquelier, C. Under Pressure: Mechanochemical Effects on Structure and Ion Conduction in the Sodium-Ion Solid Electrolyte Na_3PS_4. *J. Am. Chem. Soc.* **2020**, *142* (43), 18422–18436.

(42) Sharma, R.; Dai, Z.; Gao, L.; Brenner, T. M.; Yadgarov, L.; Zhang, J.; Rakita, Y.; Korobko, R.; Rappe, A. M.; Yaffe, O. Elucidating the Atomistic Origin of Anharmonicity in Tetragonal $CH_3NH_3PbI_3$ with Raman Scattering. *Physical Review Materials* **2020**, *4* (9), 092401.

(43) Gupta, M. K.; Ding, J.; Osti, N. C.; Abernathy, D. L.; Arnold, W.; Wang, H.; Hood, Z.; Delaire, O. Fast Na Diffusion and Anharmonic Phonon Dynamics in Superionic Na_3PS_4. *Energy Environ. Sci.* **2021**, *14* (12), 6554–6563.

(44) Chudley, C. T.; Elliott, R. J. Neutron Scattering from a Liquid on a Jump Diffusion Model. *Proc. Phys. Soc.* **1961**, *77* (2), 353–361.

(45) Freude, D.; Haase, J. Quadrupole Effects in Solid-State Nuclear Magnetic Resonance. *Special Applications* **1993**, 1–90.

(46) Harmening, T.; Eckert, H.; Pöttgen, R. Defects in Half-Heusler Type Antimonides ScTSb (T= Ni, Pd, Pt). *Solid state sciences* **2009**, *11* (4), 900–906.

(47) Radzieowski, M.; Block, T.; Koppe, J.; Hansen, M. R.; Pöttgen, R.; Janka, O. (Pseudo) Binary Antimonides: Insights on Local Ordering and Effective Charge Configurations from 121Sb MAS NMR and Mössbauer Spectroscopies. *The Journal of Physical Chemistry C* **2021**, *125* (2), 1454–1466.

(48) Brenner, T. M.; Grumet, M.; Till, P.; Asher, M.; Zeier, W. G.; Egger, D. A.; Yaffe, O. Anharmonic Lattice Dynamics in Sodium Ion Conductors. *J. Phys. Chem. Lett.* **2022**, *13* (25), 5938–5945.

(49) Brenner, T. M.; Gehrmann, C.; Korobko, R.; Livneh, T.; Egger, D. A.; Yaffe, O. Anharmonic Host-Lattice Dynamics Enable Fast Ion Conduction in Superionic AgI. *Physical Review Materials* **2020**, *4* (11), 115402.

(50) Alekperov, O.; Jahangirli, Z.; Paucar, R. First-principles Lattice Dynamics and Raman Scattering in Ionic Conductor B-Ag_2S. *physica status solidi (b)* **2016**, *253* (10), 2049–2055.

(51) Chandrasekhar, H. R.; Bhattacharya, G.; Migoni, R.; Bilz, H. Infrared and Raman Spectra and Lattice Dynamics of the Superionic Conductor Li 3 N. *Physical Review B* **1978**, *17* (2), 884.

(52) Cohen, A.; Brenner, T. M.; Klarbring, J.; Sharma, R.; Fabini, D. H.; Korobko, R.; Nayak, P. K.; Hellman, O.; Yaffe, O. Diverging Expressions of Anharmonicity in Halide Perovskites. *Advanced Materials* **2022**, *34* (14), 2107932.

(53) Cowley, R. A. Temperature Dependence of a Transverse Optic Mode in Strontium Titanate. *Physical Review Letters* **1962**, *9* (4), 159.

(54) Cochran, W. Crystal Stability and the Theory of Ferroelectricity. *Physical Review Letters* **1959**, *3* (9), 412.

(55) Jang, M. S.; Park, H. L.; Kim, J. N.; Ro, J. H.; Park, Y. H. Raman Spectrum in Monoclinic BiVO4. *Japanese Journal of Applied Physics* **1985**, *24* (S2), 506.

(56) Blinc, R. The Soft Mode Concept and the History of Ferroelectricity. *Ferroelectrics* **1987**, *74* (1), 301–303.

(57) Sharma, R.; Dai, Z.; Gao, L.; Brenner, T. M.; Yadgarov, L.; Zhang, J.; Rakita, Y.; Korobko, R.; Rappe, A. M.; Yaffe, O. Elucidating the Atomistic Origin of Anharmonicity in Tetragonal CH 3 NH 3 PbI 3 with Raman Scattering. *Physical Review Materials* **2020**, *4* (9), 092401.

(58) Yang, R. X.; Skelton, J. M.; Da Silva, E. L.; Frost, J. M.; Walsh, A. Spontaneous Octahedral Tilting in the Cubic Inorganic Cesium Halide Perovskites CsSnX3 and CsPbX3 (X= F, Cl, Br, I). *The journal of physical chemistry letters* **2017**, *8* (19), 4720–4726.

(59) Schilcher, M. J.; Robinson, P. J.; Abramovitch, D. J.; Tan, L. Z.; Rappe, A. M.; Reichman, D. R.; Egger, D. A. The Significance of Polarons and Dynamic Disorder in Halide Perovskites. *ACS Energy Letters* **2021**, *6* (6), 2162–2173.

(60) Irvine, J. T. S.; Sinclair, D. C.; West, A. R. Electroceramics: Characterization by Impedance Spectroscopy. *Adv. Mater.* **1990**, *2* (3), 132–138.

(61) Heere, M.; Hansen, A.-L.; Payandeh, S.; Aslan, N.; Gizer, G.; Sørby, M. H.; Hauback, B. C.; Pistidda, C.; Dornheim, M.; Lohstroh, W. Dynamics of Porous and Amorphous Magnesium Borohydride to Understand Solid State Mg-Ion-Conductors. *Scientific reports* **2020**, *10* (1), 1–11.

(62) Zhang, Q.; Zhang, C.; Hood, Z. D.; Chi, M.; Liang, C.; Jalarvo, N. H.; Yu, M.; Wang, H. Abnormally Low Activation Energy in Cubic Na3SbS4 Superionic Conductors. *Chemistry of Materials* **2020**, *32* (6), 2264–2271.

(63) Shimoda, M.; Maegawa, M.; Yoshida, S.; Akamatsu, H.; Hayashi, K.; Gorai, P.; Ohno, S. Controlling Defects to Achieve Reproducibly High Ionic Conductivity in Na3SbS4 Solid Electrolytes. *Chem. Mater.* **2022**, *34* (12), 5634–5643.

(64) Bloernbergen, N.; Purcell, E. M.; Pound, R. V. Relaxation Effects in Nuclear Magnetic Resonance Absorbtion. *Phys Rev* **1948**, *73* (7), 679.

(65) Arbi, K.; Lazarraga, M. G.; Ben Hassen Chehimi, D.; Ayadi-Trabelsi, M.; Rojo, J. M.; Sanz, J. Lithium Mobility in $Li_{1.2}Ti_{1.8}R_{0.2}(PO_4)_3$ Compounds (R= Al, Ga, Sc, In) as Followed by NMR and Impedance Spectroscopy. *Chemistry of materials* **2004**, *16* (2), 255–262.

(66) Mehrer, Helmut. *Diffusion in Solids*; Springer: Berlin, 2007.

(67) Morgan, B. J. Lattice-Geometry Effects in Garnet Solid Electrolytes: A Lattice-Gas Monte Carlo Simulation Study. *Royal Society open science* **2017**, *4* (11), 170824.

(68) Culver, S. P.; Squires, A. G.; Minafra, N.; Armstrong, C. W. F.; Krauskopf, T.; Böcher, F.; Li, C.; Morgan, B. J.; Zeier, W. G. Evidence for a Solid-Electrolyte Inductive Effect in the Superionic Conductor $Li_{10}Ge_{1-x}Sn_xP_2S_{12}$. *J. Am. Chem. Soc.* **2020**, *142* (50), 21210–21219.

For table of contents only